



## Bursting and spiking activities in a Wilson neuron circuit with memristive sodium and potassium ion channels

Quan Xu<sup>a</sup>, Kai Wang<sup>a</sup>, Mo Chen<sup>a</sup>, Fatemeh Parastesh<sup>b</sup>, Ning Wang<sup>a,\*</sup>

<sup>a</sup> School of Microelectronics and Control Engineering, Changzhou University, Changzhou 213159, PR China

<sup>b</sup> Centre for Nonlinear Systems, Chennai Institute of Technology, Chennai 600069, Tamil Nadu, India

### ARTICLE INFO

#### Keywords:

Bursting activity  
Spiking activity  
Memristor  
Ion channel  
Wilson neuron circuit  
Hardware experiment

### ABSTRACT

The marvelous Wilson neuron model involves sodium and potassium ion currents, which offer great significance in generating firing activities. This paper firstly deduces that the sodium ion currents can be characterized by a locally active memristor (LAM) and the potassium ion current meets the definition of passive memristor. Thereafter, a memristive Wilson neuron circuit with memristive sodium and potassium ion channels is built and its equilibrium state stability is disclosed. Dynamical explorations display that the memristive Wilson neuron circuit can generate abundant periodic bursting activities with different periodicities under low-frequency stimulus and chaotic/periodic spiking activities under high-frequency stimulus. Particularly, the bifurcation mechanisms for generating the periodic bursting behaviors are uncovered, they are Hopf/fold and fold/fold bifurcations. Besides, the memristive Wilson neuron circuit can generate chaotic and periodic bubbles with Type-I. To physically confirm these periodic bursting and chaotic/spiking activities, a discrete circuit component-based hardware experiment is executed. The experimental results effectively addressed the validity of the numerical explorations and further exhibit the effectiveness of the memristive Wilson neuron circuit in reproducing neuron bursting and spiking activities.

### 1. Introduction

Neuron circuit can effectively reproduce firing activities of an excitable neuron [1,2], which is the hardware embodiment for exploring firing activity-based artificial applications [3,4]. Diversity of firing activities and feasibility of hardware implementation are two crucial aspects for developing neuron circuits [4,5]. To date, two main categories of neuron circuits were constructed. One category was built by membrane theory, which employs capacitor and time-varying resistors to respectively characterize the electrophysiology property of a neuron membrane and ion channels, e.g., Hodgkin-Huxley circuit [1,6]. This category of neuron circuit can effectively reproduce firing activities of a biological neuron and reflects the forming process of an action potential, e.g., the evolution process of depolarization, repolarization, hyperpolarization, and after depolarization [7,8]. The other category was built by dynamical assumption, which frequently involves capacitor and nonlinear circuit elements. This category neuron circuit, e.g., FitzHugh-Nagumo circuit [9,10], can generate abundant neuron-like firing activities [11]. Summarily, the neuron circuits built by membrane theory can more preciously reproduce firing activities of an excitable biological

neuron.

The marvelous Wilson neuron model is the simplified version of the Hodgkin-Huxley neuron model, which only involves sodium and potassium ion currents [12]. The sodium ion channel is only depicted by a voltage-controlled current. From the viewpoint of circuit theory, the sodium ion channel is only depicted by a voltage-controlled nonlinear resistor. This is very different from the sodium ion channel description in the Hodgkin-Huxley circuit, which is a time-varying resistor [13]. Indeed, it has been verified that the time-varying resistor for sodium ion channel is a LAM in Hodgkin-Huxley circuit, which plays a vital role in providing energy for the depolarization process for generating an action potential [14]. That is, numerous sodium ions move inwards from outside to inside the neuron membrane inducing the increase of membrane potential. The potassium ion current is not only controlled by the membrane potential, but also related to the recovery variable. In fact, this meets the definition of a memristor [15]. Thus, the potassium ion current can be depicted by a memristor from the circuit theory viewpoint. Actually, numerous potassium ions move outwards from the inside to outside the neuron membrane during the polarization process. In this process, the membrane potential decrease, e.g., action potential

\* Corresponding author.

E-mail address: [cczuwangning@163.com](mailto:cczuwangning@163.com) (N. Wang).

<https://doi.org/10.1016/j.chaos.2024.114654>

Received 26 January 2024; Received in revised form 21 February 2024; Accepted 22 February 2024

Available online 1 March 2024

0960-0779/© 2024 Elsevier Ltd. All rights reserved.

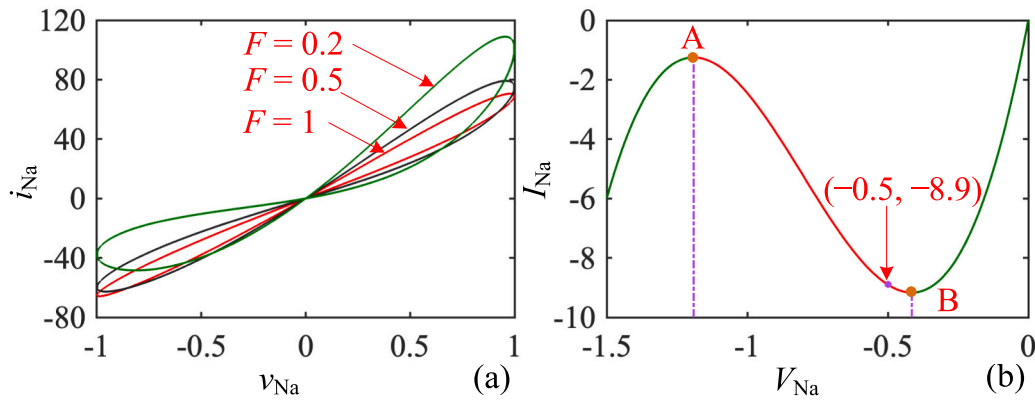


**Fig. 1.** Inner properties of the memristor describing the sodium ion channel: (a) Frequency-dependent pinched hysteresis loops with  $V_m = 1$ ; (b) DC  $V-I$  curve with negative slope for AB segment (local active domain) in the  $V_{Na} - I_{Na}$  plane.

decrease. These remind us that we can employ memristors to characterize the electrophysiology properties of sodium ion and potassium ion channels to build a memristive Wilson neuron circuit.

Moreover, many scientists have paid their attention to hardware implementation of neuron circuits, which are the hardware embodiment of firing activities and benefits for firing activity-based applications [16]. Till now, various kinds of implementation technologies were employed to physically implement the neuron circuits, e.g., nanomaterial-based nanocircuit [17] and neuristor [18], silicon-based VLSI circuits [19,20] and RRAM array [21], FPGA-based [22,23] and STM32-based [24] digital platforms, and discrete circuit component-based analog circuits [25,26]. In general, the properties of material and circuit architecture should be simultaneously considered in the implementation technologies of nanomaterial-based nanocircuit and neuristor, silicon-based VLSI circuit, and RRAM array. The limitations of hardware resource, speed restriction, and accuracy should be concerned in STM32- and FPGA-based ones [27–29], but digital platforms have the advantages of easily changing system parameters and presetting initial conditions [30]. Thinking about it on as whole and taking the advantages of better designing flexibility and real-time [31], discrete circuit components-based analog implementation requires less experimental equipment and more suitable for doing validation for numerical simulation. Thus, we will employ discrete circuit component-based hardware experiment in this paper.

In the literature, neuron-like bursting and spiking activities have been explored in neuron models [32,33], Josephson junction [34], and electronic circuit [35], just to name a few. The bursting activity was frequently demonstrated in slow-fast systems referring to fold and Hopf bifurcations, which can be employed to analyze the forming mechanism of bursting behaviors [33]. Certainly, firing activities are not limited to these. There exist some other kinds of interesting neural dynamics, e.g., stochastic resonance, which can enhance the detection ability of weak signals in the presence of noise [36]. Beyond the neuronal dynamics in a single neuron, synchronization and chimeras of neuron-based networks [37,38] can be employed to investigate the various functional aspects of nature, e.g., animal groups, insect swarms, and brain neurons [39]. These are the hot topics in the fascinating fields for researching neuronal dynamics. In this paper, we mainly focus on exploring the bursting and spiking activities in our proposed memristive Wilson neuron circuit.

Inspired by these literature, we employ a N-type LAM [40] and a passive memristor to describe the sodium and potassium ion channels in the marvelous Wilson neuron model, thereby a memristive Wilson neuron circuit is built. The memristive Wilson neuron circuit only contains a LAM, a passive memristor, a capacitor, two reversal potentials, and an external stimulus. Stimulus-related dynamical distribution, bifurcation behavior, and firing activities of bursting and spiking behaviors are numerically explored and experimentally validated.

Different from the previously reported memristive Wilson neuron models employing the memristors as synapse and electromagnetic induction [41,42], the N-type LAM and passive memristor are directly utilized to characterize ion channels to construct memristive Wilson neuron model. This has not been reported in the literature.

The rest of this paper is given as follows: Section 2 develops the memristive Wilson neuron circuit and analyses the stability of its equilibrium state. Section 3 investigates the dynamical effects of external stimulus with low-frequency and deduces the forming mechanism of bursting behaviors. Then, high-frequency dynamical effects of spiking activities and chaotic/periodic bubbles are uncovered in Section 4. Section 5 demonstrates discrete circuit component-based hardware implementation and experimental measurement. Section 6 summaries the conclusion and draws future works.

## 2. Memristive Wilson neuron circuit

Referring to the above-mentioned inspirations, a memristive Wilson neuron circuit is firstly constructed by utilizing a N-type LAM and a passive memristor to characterize the sodium and potassium ion currents in the original Wilson neuron model, respectively. Then, the state equation of the memristive Wilson neuron circuit is given, upon which the equilibrium state and its stability are demonstrated.

### 2.1. Simple review for the Wilson neuron model

The original Wilson neuron model is depicted by two first-order differential equations, which is a simplified version of the Hodgkin-Huxley neuron model [12]. The original 2D Wilson neuron model is written as

$$\begin{cases} C_m \frac{dv}{dt} = -m_\infty(v)(v - E_{Na}) - g_K r(v - E_K) + I, \\ \frac{dr}{dt} = \frac{1}{\tau_r} (-r + r_\infty(v)), \end{cases} \quad (1)$$

where  $C_m$  is the membrane capacitor with its voltage  $v$ , also known as membrane potential.  $r$  is recovery variable to describe the potassium ion in bringing back the neuron to resting state.  $E_{Na}$  and  $E_K$  are reversal potentials for the sodium and potassium ion channels, respectively.  $g_K$  is maximum conductance of potassium ion channel.  $I$  is an external stimulus.  $\tau_r$  depicts the time-scale constant of potassium ion channel. The typical parameters are  $C_m = 1$ ,  $\tau_r = 5$ ,  $g_K = 26$ ,  $E_{Na} = 0.5$ ,  $E_K = -0.95$ , which are normalized parameters [12].  $m_\infty(v)$  and  $r_\infty(v)$  are activation functions of the two ion channels. They are related to membrane potential and having the quadratic polynomial forms

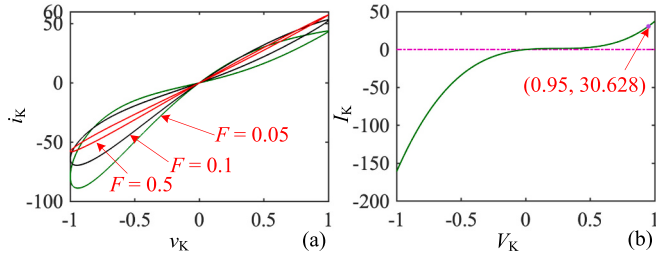


**Fig. 2.** Inner properties of the memristor describing potassium ion channel: (a) Frequency-dependent pinched hysteresis loops with  $V_m = 1$ ; (b) DC  $V - I$  curve with positive slope in the  $V_K - I_K$  plane, which declares that the memristor is passive.

$$\begin{aligned} m_\infty(v) &= 17.8 + 47.6v + 33.8v^2, \\ r_\infty(v) &= 1.24 + 3.7v + 3.2v^2. \end{aligned} \quad (2)$$

The  $m_\infty(v)(v - E_{Na})$  in Eq. (1) can be regarded as sodium ion current, which is only controlled by the membrane potential. The  $g_K r(v - E_K)$  in Eq. (1) can be regarded as potassium ion current and  $r$  can be considered as inner state for a memristor from the viewpoint of circuit theory.

## 2.2. Memristive sodium and potassium ion channels

To more precisely characterize the electrophysiological property of sodium ion channel, we propose a memristor with linear mem-conductance function and quadratic polynomial state function, which is the same as the sodium ion expression in the original Wilson neuron model. The mathematical model of the memristor is

$$\begin{cases} i_{Na} = W(\varphi_1)v_{Na}, \\ \frac{d\varphi_1}{d\tau} = -\varphi_1 + 50.05 + 81.4v_{Na} + 33.8v_{Na}^2, \end{cases} \quad (3)$$

where  $\varphi_1$  is the inner state variable and  $W(\varphi_1) = \varphi_1$  is mem-conductance of the memristor. The state equation is depicted by a quadratic polynomial state function showing in the second equation in (3) and the memristor is voltage-controlled. When a bipolar stimulus  $v_{Na} = V_m \sin(2\pi F\tau)$  is applied, the frequency-dependent pinched hysteresis loops for  $F = 0.2, 0.5, \text{ and } 1$  with  $V_m = 1$  are displayed in Fig. 1(a). One can see that the lobe area of the pinched hysteresis loop decreases with the increase of frequency, which manifests the frequency-dependent characteristics of a memristor [15].

Thereafter, we set  $i_{Na}$  to  $I_{Na}$  and  $v_{Na}$  to  $V_{Na}$  in (3) and get the relation between  $I_{Na}$  and  $V_{Na}$ , which describes the DC  $V - I$  property of the memristor. In Fig. 1(b), the DC  $V - I$  curve is figured out. Obviously, the DC  $V - I$  curve has negative slopes between point A and point B, e.g.,  $-1.1911 \leq V_{Na} \leq -0.4144$ , resp.  $-1.2473 \geq I_{Na} \geq -9.1675$ . This reflects that the memristor can provide energy when it works in the range of  $-1.1911 \leq V_{Na} \leq -0.4144$ , aka, local active domain, which is benefit for generation an action potential [43]. Note that the DC  $V - I$  curve like a 'N', which is called N-type LAM.

When the LAM working with a bias voltage, aka, a reversal potential  $E_{Na}$ , (3) can be rewritten as

$$\begin{cases} i_{Na} = \varphi_1(v - E_{Na}), \\ \frac{d\varphi_1}{d\tau} = -\varphi_1 + 50.05 + 81.4(v - E_{Na}) + 33.8(v - E_{Na})^2. \end{cases} \quad (4)$$

If we set  $E_{Na} = 0.5$ , one can get

$$\frac{d\varphi_1}{d\tau} = -\varphi_1 + m_\infty(v). \quad (5)$$

For  $d\varphi_1/d\tau = 0$ , a special case of that the sodium ion current only controlled by the membrane potential, we obtain  $\varphi_1 = m_\infty(v)$ . Then, the first equation describing the sodium ion current in (4) is the same as the one in Eq. (1). This manifests that the expression of sodium ion current

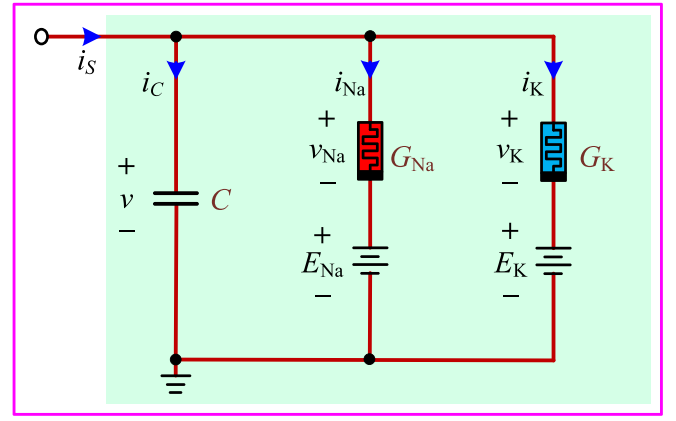


**Fig. 3.** Memristive Wilson neuron circuit containing a membrane capacitor, an external stimulus and two memristive ion channels.

in the original Wilson neuron model is a special case of our memristive sodium ion current and the LAM is working in its local active domain for  $E_{Na} = 0.5$ .

For  $E_K = -0.95$ , the potassium ion current can be rewritten as

$$\begin{cases} i_K = g_K W(\varphi_2)v_K, \\ \frac{d\varphi_2}{d\tau} = \frac{1}{\tau_r} (-\varphi_2 + 0.613 - 2.38v_K + 3.2v_K^2), \end{cases} \quad (6)$$

where the mem-conductance  $W(\varphi_2) = \varphi_2$  is a linear function.  $\varphi_2$  is the memristor inner state. To confirm its memristor property, a bipolar stimulus  $v_K = V_m \sin(2\pi F\tau)$  is applied and the frequency-dependent pinched hysteresis loops for  $F = 0.05, 0.1, \text{ and } 0.5$  with  $V_m = 1$  are displayed in Fig. 2(a). One can see that the lobe area of the pinched hysteresis loop decreases with the increase of frequency. This indicates that the potassium ion current also meets the definition of a memristor and it is voltage-controlled [15]. To investigate the DC property, we set  $i_K$  to  $I_K$  and  $v_K$  to  $V_K$  in (6) and get the relation between  $I_K$  and  $V_K$ . The DC  $V - I$  curve is figured out as shown in Fig. 2(b). Obviously, the DC  $V - I$  curve always has positive slope. This reflects that the memristor describing potassium ion current in Wilson neuron model is passive.

## 2.3. Modeling and stability analysis

By fully considering the aforementioned thoughts, we firstly construct a memristive Wilson neuron circuit with a N-type LAM and a passive memristor to characterize the electrophysiological properties of sodium and potassium ion channels. The memristive Wilson neuron circuit involves a N-type LAM  $G_{Na}$ , a passive memristor  $G_K$ , two reversal potentials  $E_{Na}$  and  $E_K$ , a capacitor  $C$ , and an AC external stimulus  $i_s$ , as shown in Fig. 3. Herein, we maintain the two reversal potentials  $E_{Na} = 0.5$  and  $E_K = -0.95$ . Thus, the memristive Wilson neuron circuit is mathematically modeled as

$$\begin{cases} C_m \frac{dv}{d\tau} = -\varphi_1(v - 0.5) - g_K \varphi_2(v + 0.95) + i_s, \\ \frac{d\varphi_1}{d\tau} = -\varphi_1 + m_\infty(v), \\ \frac{d\varphi_2}{d\tau} = \frac{1}{\tau_r} [-\varphi_2 + r_\infty(v)], \end{cases} \quad (7)$$

where  $i_s = I_m \sin(\Omega\tau)$  having amplitude  $I_m$  and angular frequency  $\Omega$ . Thus, the circuit state equation described by (7) is a three-dimensional non-autonomous dynamical system. Eq. (7) can be utilized to study the equilibrium state stability and reveal the dynamical behavior of the memristive Wilson neuron circuit.

The equilibrium state of (7) can be deduced as

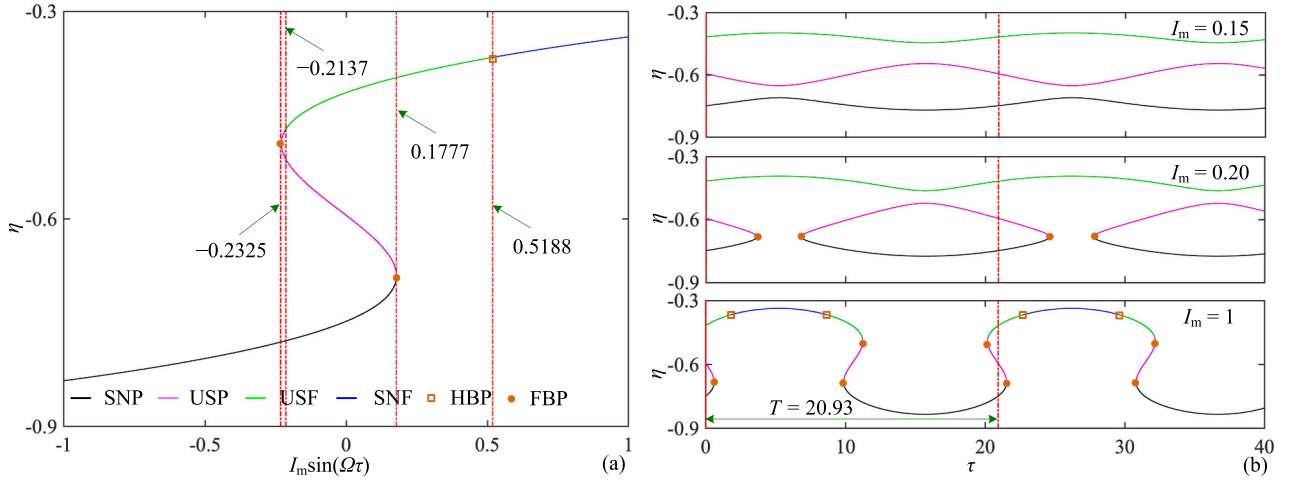


**Fig. 4.** Equilibrium state evolution and stability distribution: (a) Evolution with external stimulus. The memristive Wilson neuron circuit possess three equilibrium states and they are independent when  $I_m < 0.1777$ , one or three equilibrium states when  $0.1777 < I_m < 0.2317$ , and one or three equilibrium states when  $I_m > 0.2325$ ; (b) Evolution with the time for three paradigms, they are  $I_m = 0.15$  in  $I_m < 0.1777$ ,  $I_m = 0.20$  in  $0.1777 < I_m < 0.2317$ , and  $I_m = 1$  in  $I_m > 0.2325$ .

$$E_s = [\eta, 17.8 + 47.6\eta + 33.8\eta^2, 1.24 + 3.7\eta + 3.2\eta^2], \quad (8)$$

where  $\eta$  can be obtained by solving the follow equation

$$117\eta^3 + 205.94\eta^2 + 117.63\eta + 21.728 - I_m \sin(\Omega\tau) = 0. \quad (9)$$

The Jacobian matrix at equilibrium state  $E_s$  can be derived as

$$\mathbf{J}_{E_s} = \begin{bmatrix} -117\eta^2 - 143.8\eta - 50.04 & -\eta + 0.5 & -26\eta - 24.7 \\ 67.6\eta + 47.6 & -1 & 0 \\ 1.28\eta + 0.74 & 0 & -0.2 \end{bmatrix}. \quad (10)$$

According to the Jacobian matrix, the polynomial equation can be written as

$$\lambda^3 + m_1\lambda^2 + m_2\lambda + m_3 = 0, \quad (11)$$

where

$$\begin{aligned} m_1 &= 117\eta^2 + 143.8\eta + 51.24, \\ m_2 &= 241.28\eta^2 + 237.216\eta + 54.726, \\ m_3 &= 70.2\eta^2 + 82.376\eta + 23.526. \end{aligned}$$

In Fig. 4, the equilibrium state evaluates with the external stimulus

and the time are displayed. Fig. 4(a) demonstrates that the number of equilibrium states and their stability are different for  $I_m \sin(\Omega\tau)$ . The curves colored in black, magenta, green, and blue stand for stable node point (SNP), unstable saddle point (USP), unstable saddle focus (NSF), and stable node focus (SNF), respectively.  $\square$  and  $\bullet$  represent the Hopf bifurcation point (HBP) and fold bifurcation point (FBP) [44]. It is stated that the memristive Wilson neuron circuit possess three equilibrium states and they are independent when  $I_m < 0.1777$  with evolution of the time. When  $0.1777 < I_m < 0.2317$ , it has one or three equilibrium states and the USP and SNP merged and disappeared in some time range. When  $I_m > 0.2325$ , it has one or three equilibrium states and they are connected at some time. Especially, the Hopf bifurcation can occur only when  $I_m > 0.5188$ . Note that the evolution of the equilibrium state only depicts in one period of the external stimulus. Herein, three values of  $I_m$  are utilized to demonstrate the equilibrium state evolution with respect to time, they are  $I_m = 0.15$ ,  $0.20$ , and  $1$  with  $\Omega = 0.3$  (period  $T = 20.93$ ), as shown in Fig. 4(b). They display that there exist three independent equilibrium states for  $I_m = 0.15$ , indicating that no bifurcation occurs. There exist one or three equilibrium states, for which the USF is independent and the USP and SNP merged and disappeared in some time

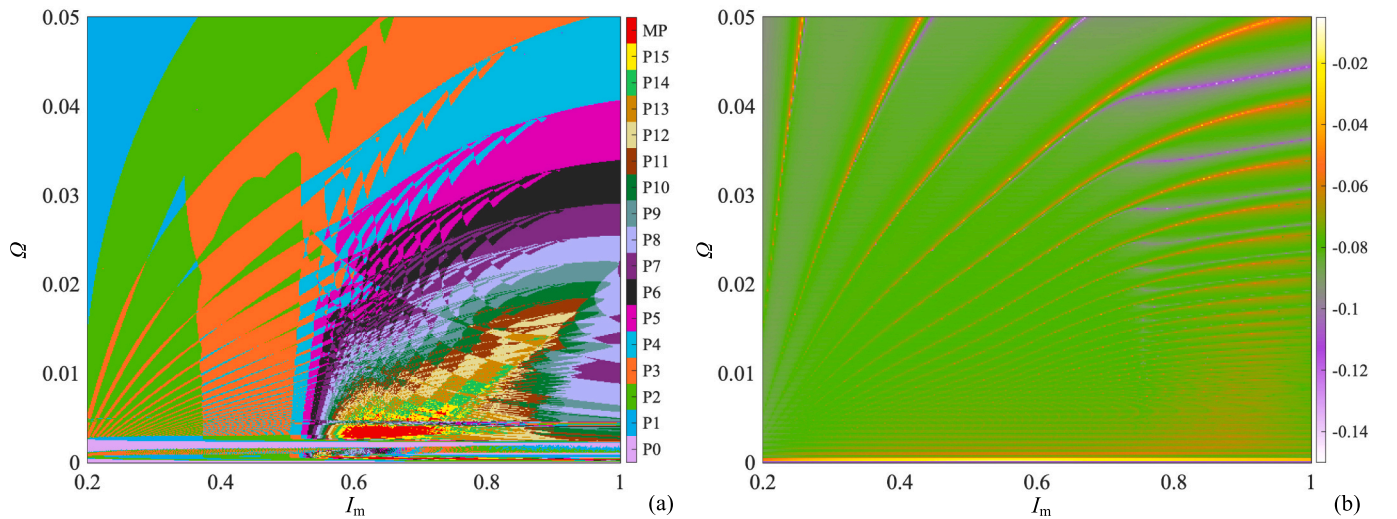


**Fig. 5.** Double-parameter dynamical distribution in the  $I_m - \Omega$  parameter plane: (a) Bifurcation diagram acquired by checking the periodicity for time-domain sequence of membrane potential  $v_i$ , which is painted by different colors to distinguish periodic states with different periodicities; (b) LLE distribution and all the LLEs are negative in the considered parameter range.

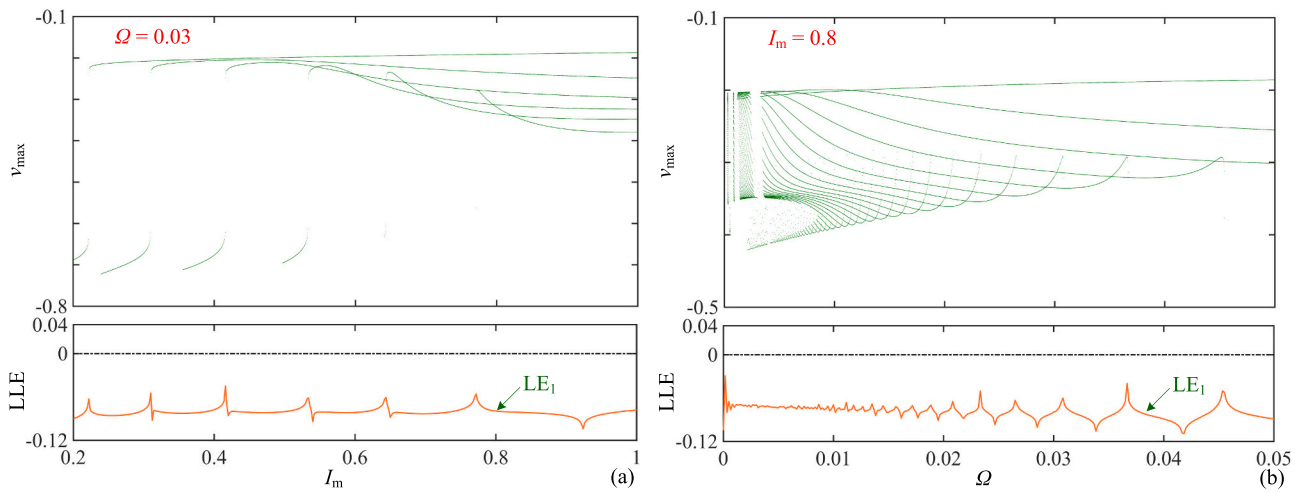


**Fig. 6.** Single-parameter bifurcation behaviors with variations of  $I_m$  and  $\Omega$ , respectively: (a) Bifurcation diagram (up) described by the maximum value of membrane potential  $v_{\max}$  and LLE (bottom) for  $I_m$  changing in  $0.2 \leq I_m \leq 1$ ; (b) Bifurcation diagram (up) and LLE (bottom) for  $\Omega$  changing in  $0 \leq \Omega \leq 0.05$ .

range for  $I_m = 0.2$ , which leads to the occurrence of FBP. For  $I_m = 1$ , the three equilibrium state trajectories are connected into one, but there have one or three equilibrium states with respect to the time. The evolution of USF to SNF leading to the occurrence of Hopf bifurcation and vice versa [45]. Note that the evolution law has no concern with the angular frequency, which only influences the rate of evolution of the equilibrium state. In general, the complex equilibrium state evolution with HBP and FBP might trigger the bursting behavior in our proposed memristive Wilson neuron circuit if there exists fast-slow effect, i.e., external stimulus with very low frequency.

### 3. Dynamical effect of low-frequency stimulus

We numerically examine the dynamical behaviors of the memristive Wilson neuron circuit with low-frequency stimulus, i.e.,  $\Omega$  in the range of  $[0, 0.05]$  in this section. That is, the frequency of the external stimulus has magnitude difference versus to the internal natural frequency of a circuit. For numerical explorations, MATLAB-based ODE45 algorithm with fixed time-step 0.01 s and time-end 3000 s is adopted to simulate bifurcation diagram and Jacobi matrix-based Wolf's method [46] with time-step 1 s and time-end 20,000 s is utilized to calculate Lyapunov exponent spectrum. The initial states are assigned as  $[v(0), \varphi_1(0), \varphi_2(0)] = [0, 0, 0]$  with the consideration of eliminating the dynamical effect of initial state.

#### 3.1. Dynamical distribution and period-adding bifurcation

Dynamical distribution depicted by doubling-parameter bifurcation diagram can well display the distribution of firing activities in the double parameters plane. By checking the periodicity of membrane potential  $v$ , double-parameter bifurcation diagram in the  $I_m - \Omega$  parameter plane is obtained, as shown in Fig. 5(a). The bifurcation diagram shows that the memristive Wilson neuron circuit runs in periodic states with different periodicities in the considered parameter ranges, e.g.,  $0.2 \leq I_m \leq 1$  and  $0 \leq \Omega \leq 0.05$ . These periodic states are marked by different colors in the parameter plane, which only distinguish period-1 (P1) to period-15 (P15). The periodic states with their periodicities  $>15$  are marked by multiple period (MP). Thereafter, largest Lyapunov exponents (LLEs) with respect to the two parameters are depicted in the  $I_m - \Omega$  parameter plane, as shown in Fig. 5(b). One can see that the LLEs are all negative in the considered parameter ranges, which confirm the periodic states revealed by double-parameter bifurcation diagram. Note that the LLE is positive for chaos, zero for quasi-period, and negative for period in a non-autonomous dynamical system.

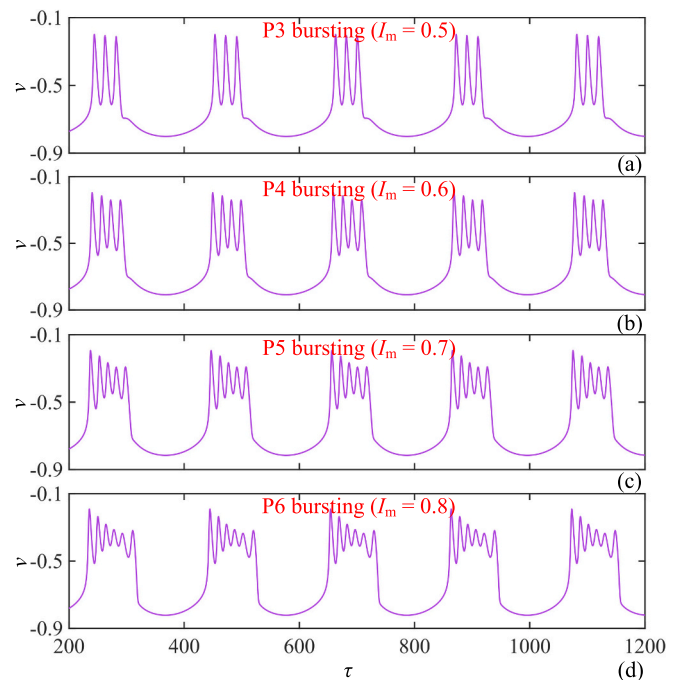


**Fig. 7.** Periodic bursting behaviors with different periodicities for different values of  $I_m$ : (a) P3 bursting for  $I_m = 0.5$ ; (b) P4 bursting for  $I_m = 0.6$ ; (c) P5 bursting for  $I_m = 0.7$ ; (d) P6 bursting for  $I_m = 0.8$ .

Single-parameter bifurcation diagram can intuitively demonstrate the transition process of firing activities with respect to a single parameter. To disclose bifurcation behaviors with respect to the two parameters of external stimulus, single-parameter bifurcation behaviors of bifurcation diagram and LLE are numerically simulated, as respectively shown in Fig. 6(a) and (b). In Fig. 6(a), the up is the single-parameter bifurcation diagram described by the maximum value of membrane potential  $v_{\max}$  and the bottom is the LLE with respect to  $I_m$  under  $\Omega = 0.03$ . One can see that period-adding bifurcation behaviors [47] is triggered with the increase of  $I_m$ , which leads to the generation of periodic states and these periodic states are confirmed by the LLE. Besides, these periodic states are bursting behaviors referring to the ones reported in the literature [48]. In Fig. 6(b), the single-parameter bifurcation behavior with respect to  $\Omega$  under  $I_m = 0.8$  is displayed, which demonstrates period-reducing bifurcation behavior with the increase of

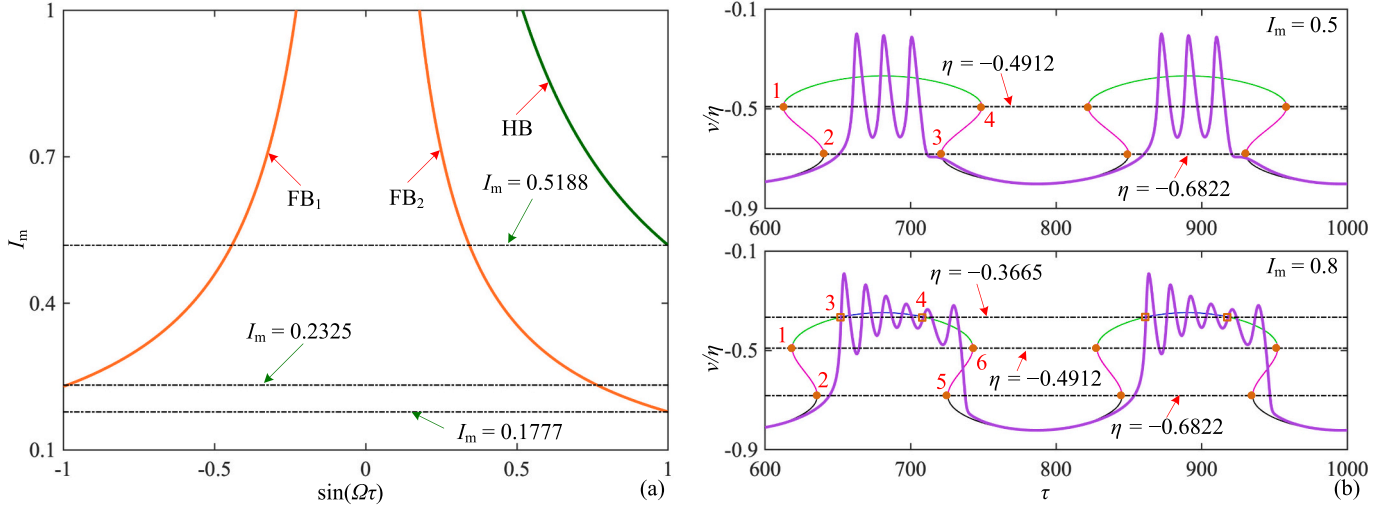


**Fig. 8.** Bifurcation sets and bifurcation mechanism: (a) The HB and FB sets in  $\sin(\Omega\tau) - I_m$  plane and there exist one FB for  $0.1777 < I_m < 0.2325$ , two FBs for  $0.2325 < I_m < 0.5188$ , and two FBs and one HB for  $I_m > 0.5188$ ; (b) Phase trajectory and equilibrium states evaluate over the time for  $I_m = 0.5$  and  $I_m = 0.8$ , respectively.

$\Omega$ . The single-parameter bifurcation diagram (up) displays periodic bursting behaviors uncountable periodicities and countable periodicities in their parameter ranges. The LLE (bottom) well verifies the periodic bursting behaviors.

To further demonstrate the periodic bursting behaviors, some values of  $I_m$  are selected from Fig. 6(a) to display the time-domain waveforms, as depicted in Fig. 7. The time-domain waveforms are P3 bursting, P4 bursting, P5 bursting, and P5 bursting for  $I_m = 0.5, 0.6, 0.7, 0.8$ , respectively. For better visualization, the time-domain waveforms only display in the time-interval [200, 1200]. One can see that the bursting rate is basically unchanged since the angular frequency of the external stimulus keeps constant, e.g.,  $\Omega = 0.03$ . The amplitude of the external stimulus regulates the spikes in each burst, but their inner forming mechanism needs to further uncover [45]. These reflect that the memristive Wilson neuron circuit can effectively produce periodic bursting behaviors and bursting frequency adaptation when applying low-frequency external stimulus. Note that periodic bursting behavior with more different periodicities can be triggered, but we only select four values of  $I_m$  as examples. As we know, the generation of bursting behavior are very related to special bifurcation behaviors, e.g., Hopf bifurcation and fold bifurcation. This will be concerned in the next subsection.

### 3.2. Bifurcation mechanism for bursting behavior

In this subsection, we deduce the fold bifurcation (FB) and Hopf bifurcation (HB) sets, and uncover the bifurcation mechanism for bursting behavior. It has been declared that the polynomial equation of a system has one zero eigenvalue manifesting the occurrence of FB [49], e.g.,  $m_3 = 0$ . Therefore, the FB set of the memristive Wilson neuron circuit is derived as

$$\text{FB} : \begin{cases} 117\eta^3 + 205.94\eta^2 + 117.63\eta + 21.728 - I_m \sin(\Omega\tau) = 0, \\ m_3 = 0. \end{cases} \quad (12)$$

The HB occurs when the polynomial equation has a pair of pure conjugate imaginary roots [45], e.g.,  $m_1 m_2 - m_3 = 0$  and  $m_3 > 0$ . There yields

$$\text{HB} : \begin{cases} 117\eta^3 + 205.94\eta^2 + 117.63\eta + 21.728 - I_m \sin(\Omega\tau) = 0, \\ m_1 m_2 - m_3 = 0, \\ m_3 > 0. \end{cases} \quad (13)$$

With references to (12) and (13), the FB and HB sets can be numerically calculated and figured out in  $\sin(\Omega\tau) - I_m$ , as shown in

Fig. 8(a). Herein, the angular frequency is set to  $\Omega = 0.03$  and the period is calculated as  $T = 209.33$ . One can see that it has one FB for  $0.1777 < I_m < 0.2325$ , two FBs for  $0.2325 < I_m < 0.5188$ , and two FBs and one HB for  $I_m > 0.5188$ . Note that the memristive Wilson neuron circuit undergoes two times of each FB and HB in a period of external stimulus as the time goes. In order to further display the bifurcation mechanism for bursting behavior, two cases are selected, e.g., **Case I** is  $I_m = 0.5$  with only two FBs and **Case II** is  $I_m = 0.8$  with two FBs and one HB. The time-domain waveform of  $v$  and trajectory of  $\eta$  are respectively plotted for  $I_m = 0.5$  (up) and  $I_m = 0.8$  (bottom), as shown in Fig. 8(b). It is worth noting that the color settings for the stability of  $\eta$ -trajectory is the same as those utilized in Fig. 4.

**Case I.** At the beginning, the circuit trajectory is in the lower resting state because the  $\eta$ -trajectory is composed of SNPs. When FB 1 occurs, the circuit trajectory deviates from the  $\eta$ -trajectory since the appearance of USPs. Then FB 2 happens, the circuit trajectory transfers to the up spiking state, since the  $\eta$ -trajectory is composed of USFs. When FB 3 occurs, the circuit trajectory drops and not to the resting state, since the appearance of USPs. When FB 4 happens, the circuit trajectory overlaps with the  $\eta$ -trajectory. Afterwards, the next cycle of this process goes.

**Case II.** At the beginning, the bifurcation mechanism is the same as the one in **Case I**. When HB 3 appears, the circuit trajectory begins to oscillate into the upper spiking state, and oscillation amplitude decreases because the  $\eta$ -trajectory is composed of SNFs. When HB 4 appears, oscillation amplitude increases because the  $\eta$ -trajectory is composed of USFs. When FB 5 and FB 6 occur, the bifurcation mechanism is the same as the one of FB 3 and FB 4 in **Case I**.

Summarily, the periodic bursting behaviors are formed by the Hopf/fold and fold/fold bifurcations in the memristive Wilson neuron circuit. The mechanisms are different with respect to the amplitude  $I_m$ . No matter which cases they are, the memristive Wilson neuron circuit can trigger abundant bursting behaviors with different periodicities.

## 4. Dynamical effect of high-frequency stimulus

To investigate the dynamical effect of external stimulus with high-frequency, we numerically reveal the dynamical distribution and bifurcation behaviors with the variation of high-frequency range, e.g.,  $0.2 \leq \Omega \leq 0.7$ . The simulation settings are identical to the ones utilized in Section 3.

The double-parameter dynamical distributions are numerically simulated in the  $I_m - \Omega$  parameter plane with the variations of  $I_m$  and  $\Omega$ ,

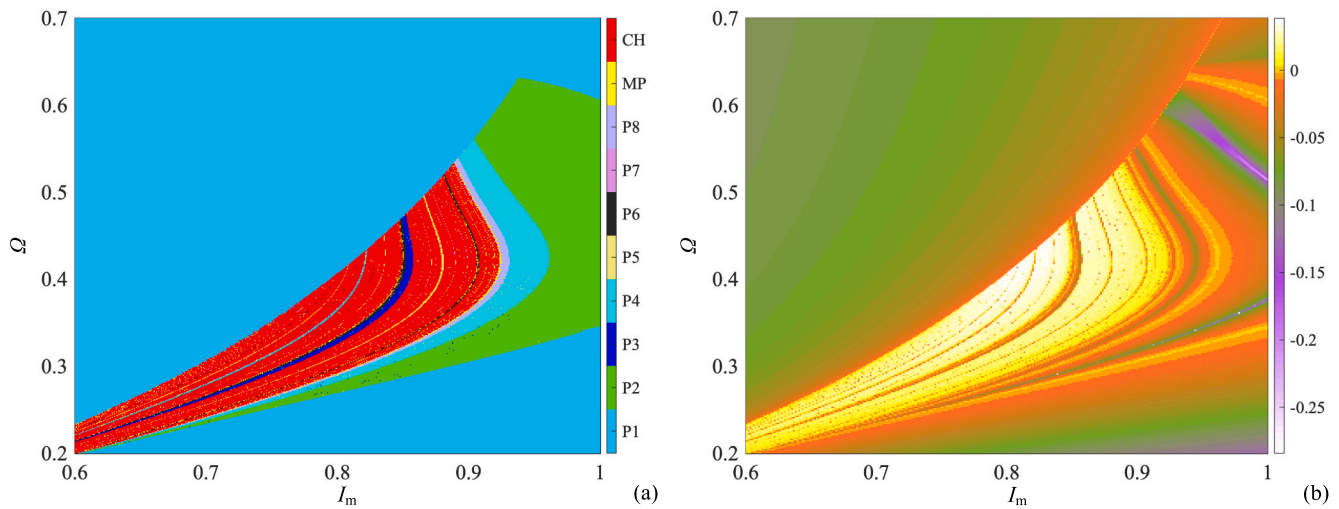


**Fig. 9.** Double-parameter dynamical distribution in the  $I_m - \Omega$  parameter plane: (a) Bifurcation diagram by checking the periodicity of membrane potential  $v$ , which is painted by different colors to distinguish states with different periodicities; (b) LLE distribution with  $LLE > 0$  for chaotic state and  $LLE < 0$  for periodic states.

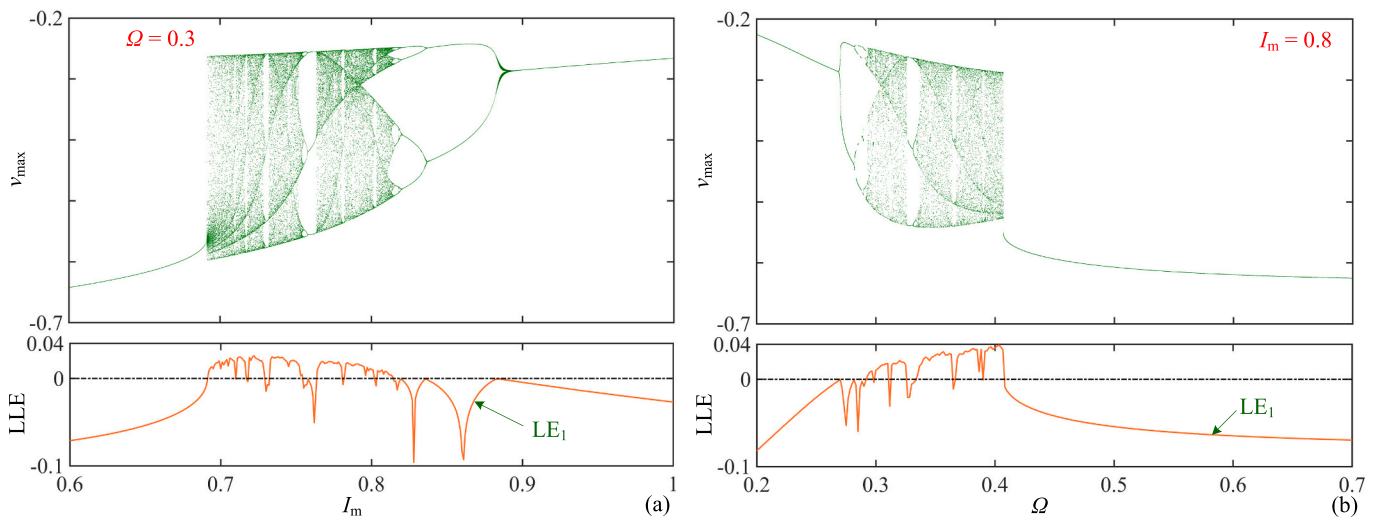


**Fig. 10.** Bifurcation behaviors with respect to  $I_m$  and  $\Omega$ , respectively: (a) Bifurcation diagram (up) described by the maximum value of membrane potential  $v_{\max}$  and LLE (bottom) for  $I_m$  changing in  $0.6 \leq I_m \leq 1$ ; (b) Bifurcation diagram (up) and LLE (bottom) for  $\Omega$  changing in  $0.2 \leq \Omega \leq 0.7$ .

e.g.,  $0.6 \leq I_m \leq 1$  and  $0.2 \leq \Omega \leq 0.7$ , as shown in Fig. 9. In Fig. 9(a), the double-parameter bifurcation diagram demonstrates that the memristive Wilson neuron circuit can produce chaotic state, periodic states of P1 to P8, and MP with its periodicity  $>8$ . These dynamical states are filled by different colors in the parameter plane, those are, red for CH, yellow for MP, and other colors for P1 to P8. One can see that the memristive Wilson neuron circuit can run in chaotic state in a relatively large parameter range and some periodic states embed in the chaotic state range, e.g., P3 colored in blue. Besides, the bifurcation distribution emerges ribbon structure and has dynamical transition of P4-P2-P1. These predict the trigger of period-doubling bifurcation route and periodic windows [50] with variation of the high-frequency stimulus. In Fig. 9(b), LLE distribution is depicted, in which the yellow parameter range has positive LLE and the other parameter ranges colored in purple-green-tangerine have negative LLE. It obviously displays that the LLE distribution well confirms the dynamical behaviors revealed by the double-parameter bifurcation diagram.

To further disclose the period-doubling bifurcation route and periodic window, we respectively simulate single-parameter bifurcation diagram and LLE with the variation of  $I_m$  and  $\Omega$ , as shown in Fig. 10. In Fig. 10(a), the single-parameter bifurcation behavior for  $0.6 \leq I_m \leq 1$

with  $\Omega = 0.3$  is demonstrated. The bifurcation diagram (up) shows that the memristive Wilson neuron circuit undergoes reverse period-doubling bifurcation routes twice and has periodic states in chaotic range, e.g., periodic windows. Besides, chaos crisis scenarios [51] happen at  $I_m = 0.6904$  and  $0.7638$  leading to the running trajectory transmit from periodic to chaotic suddenly. The LLE across zero line from negative to positive with the occurrence of chaos crisis scenario and evaluates from negative to zero and to negative for some times with the generation of reverse period-doubling bifurcation route. One can see that the LLE (bottom) well confirm these bifurcation behaviors with the variation of  $I_m$ . In Fig. 10(b), the bifurcation diagram (up) displays forward period-doubling bifurcation routes for two times with the increase of  $\Omega$ . Specially, tangent bifurcation happens at  $\Omega = 0.4067$  leading to the disappearance of chaos suddenly, for which the LLE across zero line from positive to negative. The LLE (bottom) also well verify the dynamical behaviors revealed by the single-parameter bifurcation diagram.

Herein, we select four values of  $I_m$  to plot phase trajectory and time-domain waveform to intuitively display firing activities induced by high-frequency external stimulus. The phase trajectories in the  $v - \varphi_2$  plane and time-domain waveforms of  $v$  are figured out in Fig. 11. They are

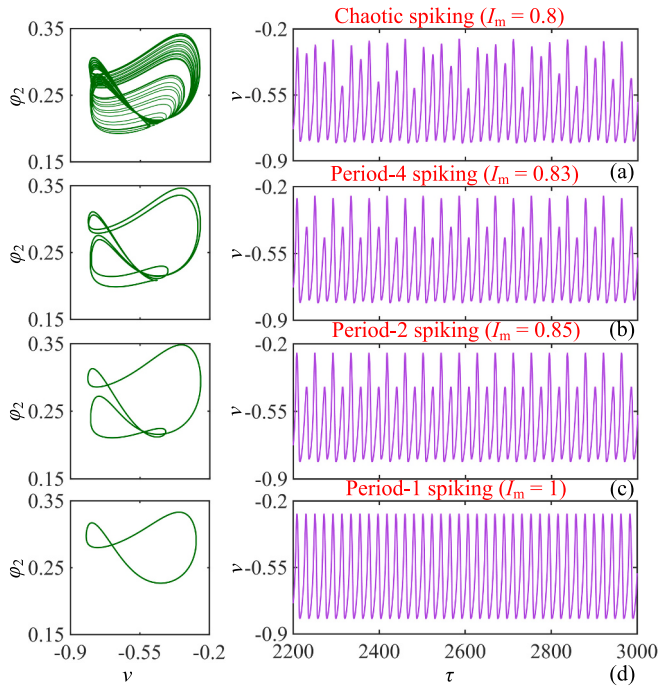


**Fig. 11.** Phase trajectory in the  $v - \varphi_2$  plane (left) and time-domain waveforms of  $v$  (right) for four different  $I_m$  with  $\Omega = 0.3$ : (a) Chaotic spiking for  $I_m = 0.8$ ; (b) Period-4 spiking for  $I_m = 0.83$ ; (c) Period-2 spiking for  $I_m = 0.85$ ; (d) Period-1 spiking for  $I_m = 1$ .

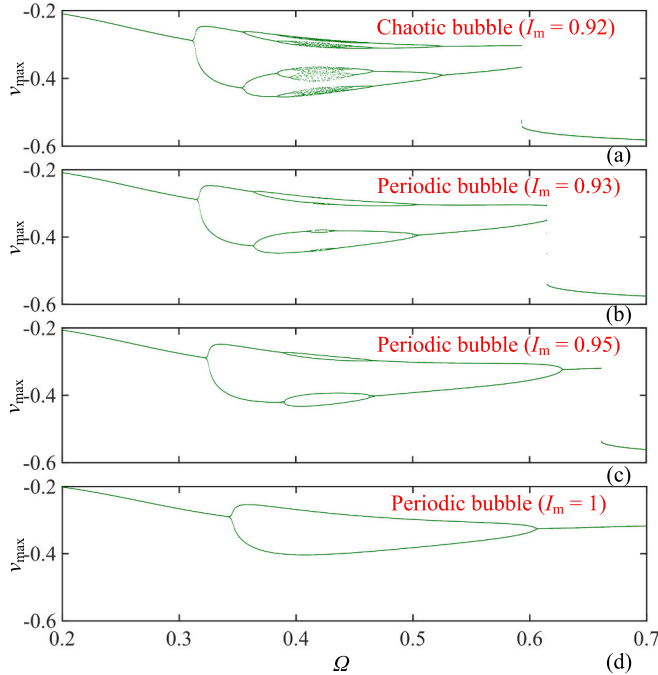


**Fig. 12.** Single-parameter bifurcation diagrams for different  $I_m$ : (a) Chaotic bubble for  $I_m = 0.92$ ; (b) Periodic bubble for  $I_m = 0.93$ ; (c) Periodic bubble for  $I_m = 0.95$ ; (d) Periodic bubble for  $I_m = 1$ .

firing activities of chaotic spiking for  $I_m = 0.8$ , period-4 spiking for  $I_m = 0.83$ , period-2 spiking for  $I_m = 0.85$ , and period-1 spiking for  $I_m = 1$ , as respectively shown in Fig. 11(a) to (d). Overall, the firing activities have a transition of CH-P4-P2-P1, which further reflects the reverse period-doubling bifurcation route with the increase of  $I_m$ . Besides, these spiking activities might hold the promise to offer high energy efficiency

implementations of spike-based neuromorphic hardware for spiking neural networks [3,21]. It is far away from potential applications, but deserves further investigations.

As shown in Fig. 9(a), one can see that the ribbon structure reflects the evolutions of P1-P2-P4-P8-CH-P8-P4-P2-P1, P1-P2-P4-P8-P4-P2-P1, P1-P2-P4-P2-P1, and P1-P2-P1 for  $I_m = 0.92, 0.93, 0.95, 1$  with the variation of  $0.2 \leq \Omega \leq 0.7$ , respectively. This demonstrates the occurrence of chaotic and periodic bubbles [52], aka, anti-monotonicity phenomenon [53]. To clearly display the anti-monotonicity, we plot single-parameter bifurcation diagrams for  $I_m = 0.92, 0.93, 0.95, 1$  with the variation of  $0.2 \leq \Omega \leq 0.7$ , as shown in Fig. 12. One can see that the bubbles possess a transition from chaotic state, to P8 state, to P4 state, to P2 state with the increase of  $I_m$ , as shown in Fig. 12(a) to (d), respectively. For each bubble, its bifurcation route undergoes forward period-doubling bifurcations and reverse period-doubling bifurcations with the increase of  $\Omega$ . Thus, these bubbles are Type-I [54].

## 5. Hardware experimental measurement

Hardware experiment is significant for verifying numerical explorations of neuron circuits [55]. We employ the discrete circuit components-based hardware to physically implement the memristive Wilson neuron circuit and perform hardware experimental measurement to verify the numerical explorations.

### 5.1. Circuit design and implementation

The emulators of LAM and passive memristor can be equivalently realized, and then the memristive Wilson neuron circuit can be implemented with the circuit schematic in Fig. 3. Floating modules realized by four current feedback operational amplifiers (CFOAs) should be employed since the involvement of two reversal potentials [16]. To solve this issue and hit the aim of achieving an optimal design and minimizing the number of discrete circuit components, we deduce the mathematical model (7) under the typical parameters and rewritten it as

$$\begin{cases} \frac{dv}{d\tau} = -\varphi_1 v + 0.5\varphi_1 - 26\varphi_2 v - 24.7\varphi_2 + I_m \sin(\Omega\tau), \\ \frac{d\varphi_1}{d\tau} = -\varphi_1 + 33.8v^2 + 47.6v + 17.8, \\ \frac{d\varphi_2}{d\tau} = -0.2\varphi_2 + 0.64v^2 + 0.74v + 0.248. \end{cases} \quad (14)$$

Eq. (14) consists of three first-order differential equations, which can be physically implemented by three integrators. The schematic of equivalent circuit is drawn in Fig. 13(a). By referring to the circuit schematic, we can easily build the circuit state equation as

$$\begin{cases} RC \frac{dV_v}{dt} = -\frac{g_1 R}{R_1} V_{\varphi_1} V_v + \frac{R}{R_2} V_{\varphi_1} - \frac{g_2 R}{R_3} V_{\varphi_2} V_v - \frac{R}{R_4} V_{\varphi_2} + \frac{R}{R_5} V_m \sin(2\pi f t), \\ RC \frac{dV_{\varphi_1}}{dt} = -\frac{R}{R_6} V_{\varphi_1} + \frac{g_3 R}{R_7} V_v^2 + \frac{R}{R_8} V_v + \frac{R}{R_9} V_1, \\ RC \frac{dV_{\varphi_2}}{dt} = -\frac{R}{R_{10}} V_{\varphi_2} + \frac{g_3 R}{R_{11}} V_v^2 + \frac{R}{R_{12}} V_v + \frac{R}{R_{13}} V_2, \end{cases} \quad (15)$$

where  $V_v, V_{\varphi_1}$ , and  $V_{\varphi_2}$  are the output voltages corresponding to  $v, \varphi_1, \varphi_2$  in numerical exploration.  $V_1$  and  $V_2$  are two DC voltages.  $g_1, g_2$ , and  $g_3$  are the gains of multipliers  $M_1, M_2$ , and  $M_3$ .  $R$  and  $C$  are integrating resistor and capacitor determining the integrating time constant  $\tau_0 = RC$ .  $V_m = I_m R_5$  and  $f = \Omega / (2\pi\tau_0)$  are the parameters of external voltage stimulus.  $R_1$  to  $R_{13}$  are resistors to regulate the coefficients in Eq. (15). By comparing Eq. (14) with Eq. (15), one can get

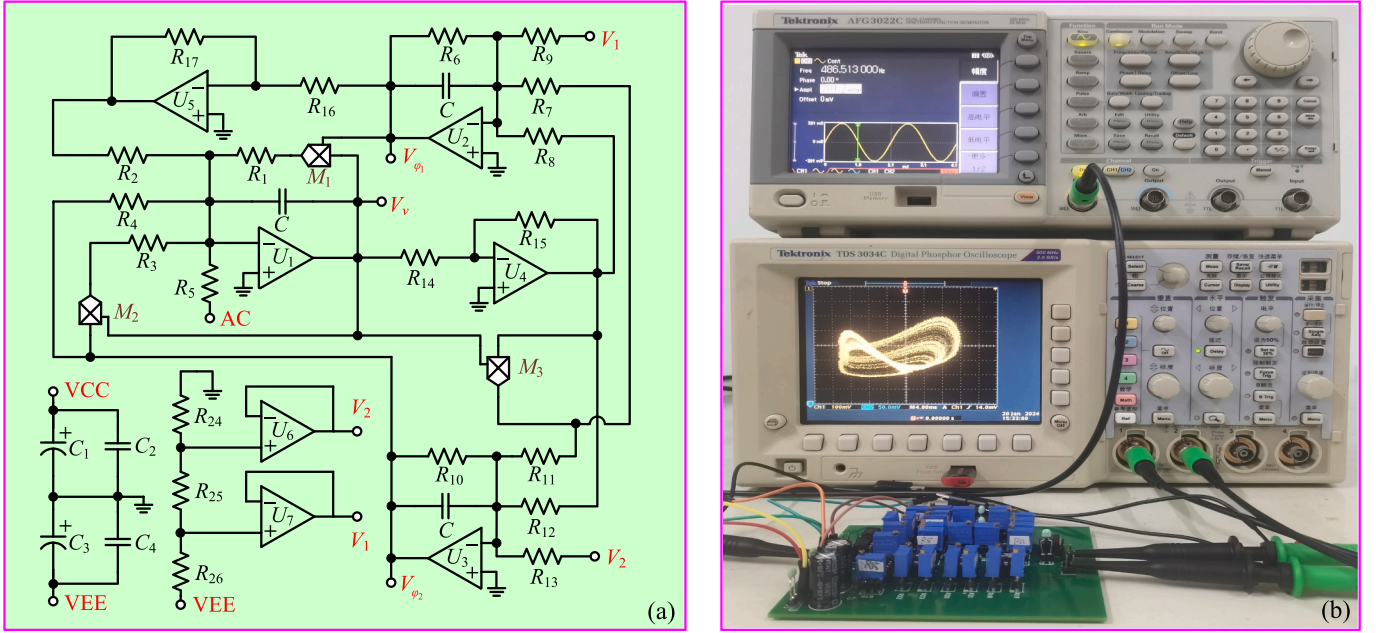


Fig. 13. Circuit design and experimental platform: (a) Circuit schematic of the memristive Wilson neuron circuit; (b) Snapshot of hardware experimental platform involving the discrete circuit component-based PCB circuit, a DC power supply, a function generator, and a digital phosphor oscilloscope.

$$\begin{aligned}
 R_1 &= g_1 R, R_2 = \frac{R}{0.5}, R_3 = \frac{g_2 R}{26}, R_4 = -\frac{R}{24.7}, R_5 = R, \\
 R_6 &= R, R_7 = \frac{g_3 R}{33.8}, R_8 = \frac{R}{47.6}, R_9 = R V_1, \\
 R_{10} &= \frac{R}{0.2}, R_{11} = \frac{g_3 R}{0.64}, R_{12} = \frac{R}{0.74}, R_{13} = R V_2.
 \end{aligned} \quad (16)$$

Note that  $U_4$  to  $U_7$  are utilized to realize two voltage inverters and two voltage followers. The two voltage inverters are employed to achieve inverse outputs of  $V_v$  and  $V_{\varphi_1}$ , respectively. The two voltage followers can insulate the DC power supplies with the main circuit. Besides, four capacitors are employed to reduce the effect of DC power supply fluctuation.

Referring to the circuit schematic in Fig. 13(a), a discrete circuit component-based PCB circuit is made and hardware experimental platform is set up, as shown in Fig. 13(b). In the hardware circuit, active circuit components of operational amplifier OP07 and analog multiplier AD633JN, as well as passive circuit components of potentiometer, electrolytic capacitor, and monolithic capacitor are utilized. Those are, OP07 for  $U_1$  to  $U_7$ , AD633JN for  $M_1$  to  $M_3$ , potentiometer for  $R_1$  to  $R_{26}$ , electrolytic capacitor for  $C_1$ ,  $C_3$ , and monolithic capacitor for  $C$ ,  $C_2$ ,  $C_4$ . Note that capacitors  $C_1$  and  $C_3$  are used to filter low and medium frequency noise and hardly filter high frequency noise, since it contains distribution inductance. Thus, capacitors  $C_2$  and  $C_4$  with small capacitance are used to filter high-frequency noise. A DC power supply, a function generator, and a digital phosphor oscilloscope are employed in setting up the hardware experimental platform.

## 5.2. Experimental measurement

We select integrating time constant  $\tau_0 = 0.1$  ms, e.g.,  $R = 10$  k $\Omega$  and  $C = 10$  nF,  $g_1 = g_2 = g_3 = 1$  V $^{-1}$ ,  $V_1 = -1.78$  V, and  $V_2 = -0.248$  V for hardware circuit. The other resistances can be calculated as  $R_1 = R_5 = R_6 = R_{13} = 10$  k $\Omega$ ,  $R_2 = 20$  k $\Omega$ ,  $R_3 = 384.62$   $\Omega$ ,  $R_4 = 404.86$   $\Omega$ ,  $R_7 = 295.86$   $\Omega$ ,  $R_8 = 210.08$   $\Omega$ ,  $R_9 = 1$  k $\Omega$ ,  $R_{10} = 50$  k $\Omega$ ,  $R_{11} = 15.625$  k $\Omega$ ,  $R_{12} = 13.514$  k $\Omega$ ,  $R_{14} \sim R_{17} = 10$  k $\Omega$ ,  $R_{24} = 248$   $\Omega$ ,  $R_{25} = 1.532$  k $\Omega$ ,  $R_{26} = 13.22$  k $\Omega$ . Note that  $R_{18} \sim R_{23}$  are utilized to control the gains of the three analog multipliers to 1 V $^{-1}$ , which are not plotted in the circuit schematic. Besides, the four filter capacitors are selected as  $C_1 = C_3 =$

Table I

Theo. values and Exp. values of stimulus parameters for low-frequency case.

Figure	$V_m$ , V		$f$ , Hz	
	Theo. value	Exp. value	Theo. value	Exp. value
Fig. 14 (a)	0.5	0.521	47.77	47.913
Fig. 14 (b)	0.6	0.635	47.77	45.826
Fig. 14 (c)	0.7	0.743	47.77	48.325
Fig. 14 (d)	0.8	0.834	47.77	48.676

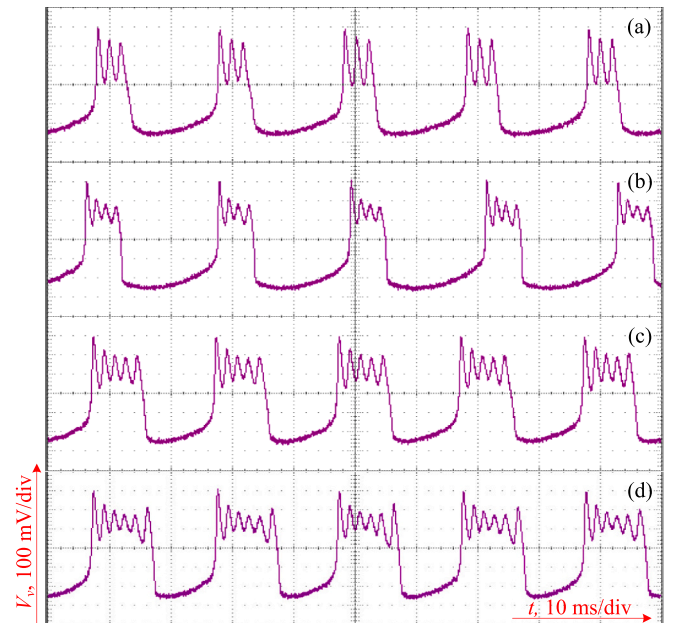


Fig. 14. Hardware measurements of time-domain waveforms of the capacitor voltage  $V_v$  for different  $V_m$ -related bursting activities: (a) P3 bursting activity; (b) P4 bursting activity; (c) P5 bursting activity; (d) P6 bursting activity.

**Table II**

Theo. values and Exp. values of stimulus parameters for high-frequency case.

Figure	$V_m, V$		$f, \text{Hz}$	
	Theo. value	Exp. value	Theo. value	Exp. value
Fig. 15 (a)	0.80	0.782	477.71	486.513
Fig. 15 (b)	0.83	0.825	477.71	489.952
Fig. 15 (b)	0.85	0.846	477.71	501.362
Fig. 15 (b)	0.1	0.983	477.71	501.362

100  $\mu\text{F}$  and  $C_2 = C_4 = 56 \text{ nF}$ . Herein, the parameters  $V_m$  and  $f$  are regulated to correspond the employment of  $I_m$  and  $\Omega$  in the numerical simulations and they are finely adjusted to make up the inevitable parasitic circuit parameters and temperature effects of the discrete circuit components [56,57].

For the low-frequency case, the theoretical (Theo.) values in numerical simulations and experimental (Exp.) values in experimental measurement of stimulus parameters  $V_m$  and  $f$  are listed in Table I. The time-domain waveforms of capacitor voltage  $V_c$  are acquired, as displayed in Fig. 14. The experimentally measured results demonstrate well consistence with the numerically simulated ones in Fig. 7. It is worth noting that the time-domain waveforms are moved up with 500 mV for better displaying the visualization of experimental results.

For the high-frequency case, the Theo. values in numerical simulations and Exp. values in experimental measurement of stimulus parameters  $V_m$  and  $f$  are listed in Table II. The phase trajectories in the  $V_c - V_{\phi 2}$  plane are captured, as displayed in Fig. 15, they are corresponding to the numerical simulations in Fig. 11. It can be seen that the experimental measurements are consistent with the numerical simulations well. Note that the phase trajectories are moved down with 250 mV and right with 500 mV for better displaying the visualization of experimental results.

The Mean Absolute Percentage Error (MAPE) method was employed to display the deviations between the measured and desired resistance [16]. The expression of MAPE is written as

$$\text{MAPE} = \frac{1}{N} \sum_{k=1}^N \frac{|P_{\text{desired}k} - P_{\text{measured}k}|}{P_{\text{desired}k}} \times 100\%, \quad (17)$$

where  $P_{\text{desired}k}$  is the expected parameters in numerical simulation and  $P_{\text{measured}k}$  is the measured parameters in hardware experiment.  $N$  is the number of fine-regulated parameters. For the time-domain waveforms and phase trajectories in Fig. 14 and Fig. 15, the MAPEs are calculated with  $N = 2$ . Those are 2.25 %, 4.95 %, 3.65 %, 3.07 % for Fig. 14(a) to Fig. 14(d) and 2.05 %, 1.58 %, 2.71 %, 3.33 % for Fig. 15(a) to Fig. 15 (d), respectively. The calculated results display that the MAPEs are all smaller than 10 %. This is acceptable in analog hardware experiment.

On the whole, the discrete circuit component-based hardware of the memristive Wilson neuron circuit can reproduce periodic bursting activities with different periodicities and chaotic/periodic spiking activities. This indicates the effectiveness of the hardware circuit in generating these firing activities. Besides, this further manifests the availability of employing a LAM and a passive memristor to characterize the electrophysiological properties of sodium and potassium ion channels in building a Wilson neuron circuit.

## 6. Conclusion

A memristive Wilson neuron circuit was firstly built in this paper, which employs a LAM and a passive memristor to respectively characterize the electrophysiological properties of sodium and potassium ion channels of a Wilson neuron model. Numerical explorations and discrete circuit component-based hardware experiments were executed, which show feasibility of the memristive Wilson neuron circuit in effectively

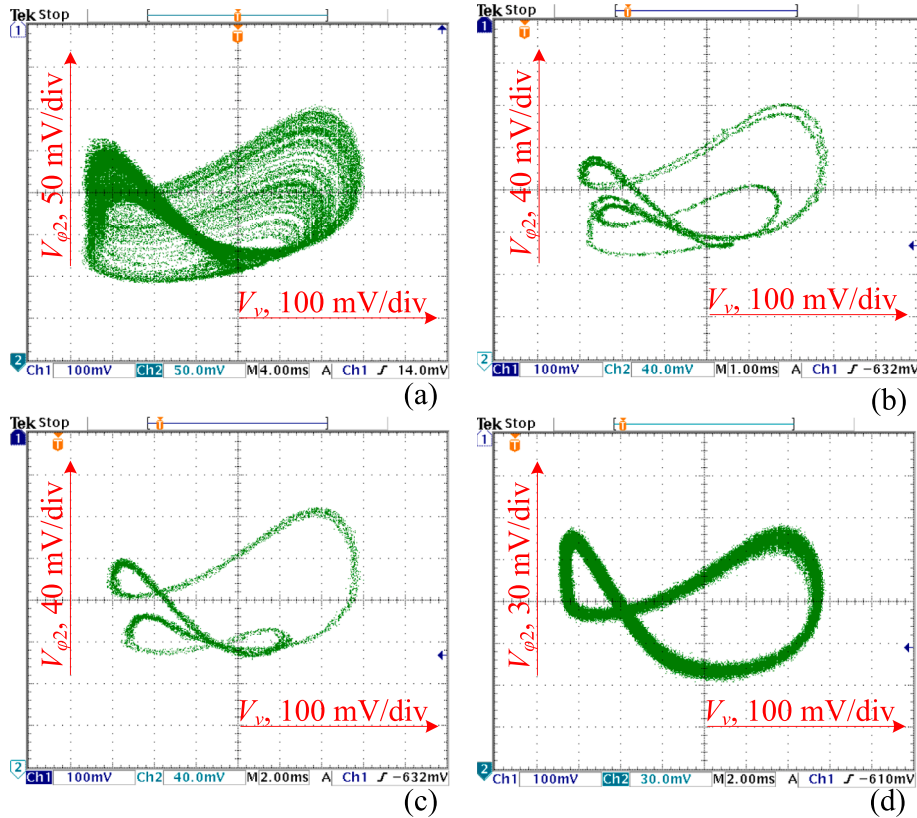


**Fig. 15.** Hardware measurements of phase trajectories in the  $V_c - V_{\phi 2}$  plane for different  $V_m$ -related spiking activities: (a) Chaotic spiking activity with 100 mV/div for Ch1 and 50 mV/div for Ch2; (b) P4 spiking activity with 100 mV/div for Ch1 and 40 mV/div for Ch2; (c) P2 spiking activity with 100 mV/div for Ch1 and 40 mV/div for Ch2; (d) P1 spiking activity with 100 mV/div for Ch1 and 30 mV/div for Ch2.

producing periodic bursting and chaotic/periodic spiking activities and availability of the discrete circuit component-based analog hardware implementation. It is of great significance that the bifurcation mechanism for generating the periodic bursting behavior were uncovered, they are Hopf/fold and fold/fold bifurcations. Besides, the memristive Wilson neuron circuit can generate chaotic and periodic bubbles with Type-I.

It has been declared that the Hodgkin-Huxley circuit is made of LAMs, in which LAMs are employed to restrict the sodium ion and potassium ion channels [13]. Different from the memristive Hodgkin-Huxley circuit, we firstly deduced that the potassium ion channel is a passive memristor in the marvelous Wilson neuron model and built a memristive Wilson neuron circuit. The done work let us know that the circuit topology is feasible to construct memristive Wilson neuron circuits with a LAM and a passive memristor to respectively characterize sodium and potassium ion channels. It is an open topic to develop LAM and passive memristor with simpler mathematical models to build a new memristive Wilson neuron circuit by referring to the circuit topology and uncover the unknown features of the memristive Wilson neuron circuit. Besides, the method for constructing the memristive potassium ion channel can be extended to build other memristive neuron models, e. g., constructing a memristor to characterize the cubic nonlinear term in FitzHugh-Nagumo neuron model. These deserve more concern.

### CRedit authorship contribution statement

**Quan Xu:** Writing – original draft, Methodology, Formal analysis. **Kai Wang:** Formal analysis, Conceptualization. **Mo Chen:** Writing – review & editing, Formal analysis. **Fatemeh Parastesh:** Software. **Ning Wang:** Writing – review & editing, Supervision, Project administration.

### Declaration of competing interest

The authors declare that they have no known competing financial interests or personal relationships that could have appeared to influence the work reported in this paper.

### Data availability

Data will be made available on request.

### Acknowledgements

This work was supported by the grants from the National Natural Science Foundations of China under Nos. 12172066, 52307002, and 52277001, the Natural Science Foundation of Jiangsu Province, China, under No. BK20230628, Centre for Nonlinear Systems, Chennai Institute of Technology, under No. CIT/CNS/2024/RP/012, and the Project 333 of Jiangsu Province.

### References

- Hodgkin AL, Huxley AF. A quantitative description of membrane current and its application to conduction and excitation in nerve. *J Physiol* 1952;117(4):500–44.
- Xu Q, Wang YT, Wu HG, Chen M, Chen B. Periodic and chaotic spiking behaviors in a simplified memristive Hodgkin-Huxley circuit. *Chaos Solit Fract* 2024;179:114458.
- Rao A, Plank P, Wild A, Maass W. A long short-term memory for AI applications in spike-based neuromorphic hardware. *Nat Mach Intell* 2022;4:467–79.
- Ying JJ, Min FH, Wang GY, et al. *Chaos Solit Fract* 2023;175:114058.
- Njitacke ZT, Ramadoss J, Takembo CN, Rajagopal K, Awrejcewicz J. An enhanced FitzHugh-Nagumo neuron circuit, microcontroller-based hardware implementation: light illumination and magnetic field effects on information patterns. *Chaos Solit Fract* 2023;167:113014.
- Hodgkin AL. The ionic basis of electrical activity in nerve and muscle. *Biol Rev* 1951;26(4):339–409.
- Wu FQ, Guo YT, Ma J. Reproduce the biophysical function of chemical synapse by using a memristive synapse. *Nonlinear Dyn* 2022;109(3):2063–84.
- Schafferhofer-Steltzer I, Hofer E, DJ HuelSing, Bishop SP, Pollard AE. Contribution of Purkinje-myocardial coupling to suppression and facilitation of early afterdepolarization-induced triggered activity. *IEEE Trans Biomed Engin* 2005;52(9):1522–31.
- Chen XJ, Wang N, Wang YT, Wu HG, Xu Q. Memristor initial-offset boosting and its bifurcation mechanism in a memristive FitzHugh-Nagumo neuron model with hidden dynamics. *Chaos Solit Fract* 2023;174:113836.
- Chen M, Qi JW, Wu HG, Xu Q, Bao BC. Bifurcation analyses and hardware experiments for bursting dynamics in non-autonomous memristive FitzHugh-Nagumo circuit. *Sci China Technol Sci* 2020;63:1035–44.
- Uludag IF, Cek ME. Spectral resonance in FitzHugh-Nagumo neuron system: relation with stochastic resonance and its role in EMG signal characterization. *Cogn Neurodyn* 2023. <https://doi.org/10.1007/s11571-023-10043-3>.
- Wilson HR. Simplified dynamics of human and mammalian neocortical neurons. *J Theor Biol* 1999;200:375–88.
- Chua LO. Memristor, Hodgkin-Huxley, and edge of chaos. *Nanotechnology* 2013;24(38):383001.
- Sah MP, Kim H, Chua LO. Brians are made of memristors. *IEEE Circuits Syst Mag* 2014;14(1):12–36.
- Chua LO. Everything you wish to know about memristors but are afraid to ask. *Radioengineering* 2015;24(2):319–68.
- Xu Q, Wang YT, HHC Iu, Wang N, Bao H. Locally active memristor based neuromorphic circuit: firing pattern and hardware experiment. *IEEE Trans Circuits Syst I* 2023;70(8):3130–41.
- Kumar S, Williams RS, Wang Z. Third-order nanocircuit elements for neuromorphic engineering. *Nature* 2020;585(7826):518–23.
- Pickett MD, Medeiros-Ribeiro G, Williams RS. A scalable neuristor built with Mott memristors. *Nat Mater* 2013;12(2):114–7.
- Yu T, Cauwenberghs G. Analog VLSI biophysical neurons and synapses with programmable membrane channel kinetics. *IEEE Trans Biomed Circuits Syst* 2010;4(3):139–48.
- Basu A, Hasler PE. Nullcline-based design of a silicon neuron. *IEEE Trans Circuits Syst I* 2010;57(11):2938–47.
- Zhou P, Eshraghian JK, Choi DU, Lu WD, Kang SM. Gradient-based neuromorphic learning on dynamical RRAM arrays. *IEEE J Emerg Selec Top Circuits Syst* 2022;12(4):888–97.
- Haghiri S, Naderi A, Ghanbari B, Ahmadi A. High speed and low digital resources implementation of Hodgkin-Huxley neuronal model using base-2 functions. *IEEE Trans Circuits Syst I* 2021;68(1):275–87.
- Lin HR, Wang CH, Yu F, Hong QH, Xu C, Sun YC. A triple-memristor Hopfield neural network with space multi-structure attractors and space initial-offset behaviors. *IEEE Trans Comput-Aided Design Integr Circuits Syst* 2023;42(12):4948–58.
- Lai Q, Lai C, Zhang H, Li CB. Hidden coexisting hyperchaos of new memristive neuron model and its application in image encryption. *Chaos Solit Fract* 2022;158:112017.
- Cai JM, Bao H, Chen M, Xu Q, Bao BC. Analog/Digital multiplierless implementations for nullcline-characteristics-based piecewise linear Hindmarsh-Rose neuron model. *IEEE Trans Circuits Syst I* 2022;69(7):2916–27.
- Sun JW, Han JT, Wang YF, Liu P. Memristor-based neural network circuit of operant conditioning accorded with biological feature. *IEEE Trans Circuits Syst I* 2022;69(11):4475–86.
- Cao HL, Wang Y, Banerjee S, Cao YH, Mou J. A discrete Chialvo-Rulkov neuron network coupled with a memristor model: design, dynamical analysis, DSP implementation and its application. *Chaos Solit Fract* 2024;179:114466.
- Mouri M, Hayati M, Serrano-Gotarredona T, Abbott D. A digital neuromorphic realization of the 2-D Wilson neuron model. *IEEE Trans Circuits Syst II* 2019;66(1):136–40.
- Imani MA, Ahmadi A, RadMalekshahi M, Haghiri S. Digital multiplierless realization of coupled Wilson neuron model. *IEEE Trans Biomed Circuits Syst* 2018;12(6):1431–9.
- Lin HR, Wang CH, Sun YC. A universal variable extension method for designing multiscroll/wing chaotic systems. *IEEE Trans Ind Electron* 2023. <https://doi.org/10.1109/TIE.2023.3299020>.
- Hu XY, Liu CX. Dynamic property analysis and circuit implementation of simplified memristive Hodgkin-Huxley neuron model. *Nonlinear Dyn* 2019;97(2):1721–33.
- Bashkirtseva I, Ryashko L, Slepukhina E. Noise-induced spiking-bursting transition in the neuron model with the blue sky catastrophe. *Phys Rev Lett* 2019;99:062408.
- Shilnikov A, Calabrese RL, Cymbalyuk G. Mechanism of bistability: tonic spiking and bursting in a neuron model. *Phys Rev E* 2005;71:056214.
- Dana SK, Sengupta D, Hu CK. Spiking and bursting in Josephson junction. *IEEE Trans Circuits Syst II* 2006;53(10):1031–4.
- Wang ZX, Zhang C, Ding ZQ, Bi QS. From period-doubling bursting to chaotic periodic in a modified Chua's circuit. *Chaos Solit Fract* 2023;174:113868.
- Palabas T, Torres JJ, Perc M, Uzuntarla M. Double stochastic resonance in neuronal dynamics due to astrocytes. *Chaos Solit Fract* 2023;168:113140.
- Hussain I, Jafari S, Ghosh D, Perc M. Synchronization and chimeras in a network of photosensitive FitzHugh-Nagumo neurons. *Nonlinear Dyn* 2021;104(3):2711–21.
- Bayani A, Jafari S, Azarnoush H, Nazarimehr F, Boccaletti S, Perc M. Explosive synchronization dependence on initial conditions: the minimal Kuramoto model. *Chaos Solit Fract* 2023;169:113243.
- Dai XF, Li XL, Gao H, Jia DY, Perc M, Manshour P, et al. Discontinuous transitions and rhythmic states in the D-dimensional Kuramoto model induced by a positive feedback with the global order parameter. *Phys Rev Lett* 2020;125:194101.
- Liang Y, Zhu Q, Wang GY, Nath SK, HHC Iu, Nandi SK, et al. Universal dynamics analysis of locally-active memristors and its applications. *IEEE Trans Circuits Syst I* 2022;69(3):1278–90.

- [41] Xu Q, Wang K, Shan YF, Wu HG, Chen M, Wang N. Dynamical effects of memristive electromagnetic induction on a 2D Wilson neuron model. *Cogn Neurodyn* 2023. <https://doi.org/10.1007/s11571-023-10014-8>.
- [42] Xu Q, Ju ZT, Ding SK, Feng CT, Chen M, Bao BC. Electromagnetic induction effects on electrical activity within a memristive Wilson neuron model. *Cogn Neurodyn* 2022;16:1221–31.
- [43] Chua LO. Hodgkin-Huxley equations implies edge of chaos kernel. *Jpn J Appl Phys* 2022;61:SM0805.
- [44] Xu Q, Chen XJ, Chen B, Wu HG, Li Z, Bao H. Dynamical analysis of an improved FitzHugh-Nagumo neuron model with multiplier-free implementation. *Nonlinear Dyn* 2023;111(9):8737–49.
- [45] Huang JJ, Bi QS. Multiple modes of bursting phenomena in a vector field of triple Hopf bifurcation with two time scales. *Chaos Solit Fract* 2023;175:113999.
- [46] Xu Q, Huang LP, Wang N, Bao H, Wu HG, Chen M. Initial-offset-boosted coexisting hyperchaos in a 2D memristive Chialvo neuron map and its application in image encryption. *Nonlinear Dyn* 2023;111(21):20447–63.
- [47] Kafraj MS, Parastesh F, Jafri S. Firing patterns of an improved Izhikevich neuron model under the effect of electromagnetic induction and noise. *Chaos Solit Fract* 2020;137:109782.
- [48] Wang XJ, Gu HG, Jia YB. Nonlinear mechanism for enhanced and reduced bursting activity respectively induced by fast and slow excitatory autapse. *Chaos Solit Fract* 2023;166:112904.
- [49] Wouapi MK, Fotsin BH, EBM Naouonkadi, Kemwoue FF, Njitacke ZT. Complex bifurcation analysis and synchronization optimal control for Hindmarsh-Rose neuron model under magnetic flow effect. *Cogn Neurodyn* 2020;15:315–47.
- [50] Lin HR, Wang CH, Sun YC, Yao W. Firing multistability in a locally active memristive neuron model. *Nonlinear Dyn* 2020;100(4):3667–83.
- [51] Meehan PA. Prediction and suppression of chaotic instability in brake squeal. *Nonlinear Dyn* 2021;107(4):205–25.
- [52] Sursh K, Prasad A, Thamilmaran K. Birth of strange nonchaotic attractors through formation and merging of bubbles in a quasiperiodically forced Chua's oscillator. *Phys Lett A* 2013;377:612–21.
- [53] Njitacke ZT, Kengne J, Kengne K. Antimonotonicity, chaos and multiple coexisting attractors in a simple hybrid diode-based Jerk circuit. *Chaos Solit Fract* 2017;105:77–91.
- [54] Cheng YZ, Min FH, Rui Z, Dou YP. Firing multistability, symmetry, bubbles of a Shinriki oscillator with mem-elements. *Chin J Physiol* 2021;74:157–74.
- [55] Minati L, Mancinelli M, Frasca M, Bettotti P, Pavesi L. An analog electronic emulator of non-linear dynamics in optical microring resonators. *Chaos Solit Fract* 2021;153:111410.
- [56] Minati L. Simulation versus experiment in non-linear dynamical systems. *Chaos Solit Fract* 2021;144:110656.
- [57] Li ZJ, Zhou HY, Wang MJ, Ma ML. Coexisting firing patterns and phase synchronization in locally active memristor coupled neurons with HR and FN models. *Nonlinear Dyn* 2021;104(2):1455–73.